Robust control for convection suppression in a fluid layer: The effects of boundary properties, actuator lag, and major parameter uncertainties

A. C. Or and J. L. Speyer
Department of Mechanical and Aerospace Engineering, University of California, Los Angeles, California 90095-1597, USA
(Received 22 October 2005; published 19 April 2006)

The robustness of control is a requirement to maintain a fluid layer at conductive equilibrium heated to a highly supercritical condition. Robustness determines how much uncertainties, or design parameter mismatches, can be tolerated. Both linear stability analysis and three-dimensional fully nonlinear simulations are used for the study of the linear quadratic Gaussian (LQG) controller. The parameter mismatches from the nominal conditions are introduced into the plant model, while the LQG compensator assumes nominal conditions. The mismatches arise from boundary properties, actuator lag, sensor level uncertainty, and wall thickness, as well as from the major parameters such as Prandtl number, Rayleigh number, wave number, and truncation number in the reduced-order model. The results suggest that the LQG compensator action can preserve closed-loop stability at over ten times the critical Rayleigh number, provided that the mismatches in the sensor level and wall thickness are small. Mismatches in the Prandtl number and wall material properties have little impact. Mismatches in Rayleigh number and wave number are relatively benign compared with the sensor and thickness parameters. Techniques for measuring the plant output temperature at multiple levels with sufficient accuracy may be an implementation challenge.

DOI: 10.1103/PhysRevE.73.046307 PACS number(s): 47.20.Bp

I. INTRODUCTION

Fluid flow control has become a rapidly growing area of research, that combines traditional knowledge of fluid dynamics and numerical computations and modern estimation and control theory. A particular well-known problem that has been pursued by investigators with interest in recent years is the convection suppression in a layer of fluid at supercritical condition (a simple two degree-of-freedom analogy is controlling an inverted pendulum about its vertical position).

The goal of analysis is to develop a robust compensator design for convection suppression using a modern control synthesis approach. The Boussinesq model of Rayleigh-Bénard convection has been investigated quite vigorously because the experimental configuration can be modeled and simulated with high fidelity. In Refs. [1,2] a purely proportional feedback control law is shown to produce encouraging results, even though the control law is well known for its limitations. Another limitation is the choice and placement of temperature sensors, Howle [1,3] measured the mean temperature, averaged over the fluid depth (by shadowgraph technique); Tang and Bau [2,4] measured the temperature only at a single level along the fluid depth. Neither has provided temperature measurements sufficient to characterize the disturbance mode shapes along the direction of the layer depth. The mixed findings, discrepancies between theoretical and experimental results reported by the authors, may very well be due to the lack of robustness of control, the simple feedback control law, as well as the crude sensor outputs and lack of observability.

Measuring disturbance temperatures at multiple levels improves the system observability significantly. In our model, knowledge of temperatures at three interior levels of the fluid layer is assumed. This is a significant assumption. For an actual laboratory implementation, the remote infrared (IR) sensing technique is probably the only viable way to acquire such knowledge. Furthermore, for a complete horizontal coverage of the fluid layer, it will probably require a high-frequency scanning and sensing technique. This technique is available for many applications but is not investigated in this study.

To improve the robustness of control we have developed a linear quadratic Gaussian (LQG) control synthesis compensator [5]. The LQG design with loop transfer recovery (LTR) is well known and proven to give robust performance in many applications. The LQG-LTR compensator is applied to a three-dimensional, fully nonlinear model [6] developed based on a Boussinesq system of equations treated by a spectral, time-splitting technique (see Marcus [7]). The results show that the linear compensator is effective in damping out an initial state of finite-amplitude convection at a higher Ra than that reported in Refs. [1,4]. The linear compensator is modally distributed. Although the compensator built for each Fourier mode is linear, controlling all Fourier harmonic modes is nonlinear in the sense that all these modes are generated by the advective nonlinearities. Two further significant advances in the compensator design are reported in Ref. [8]. These are (i) the successful building of an order-reduced LQG compensator, and (ii) the developing of a gain schedule algorithm.

This paper aims at the robustness of the LQG compensator. To enhance the fidelity of the existing plant models (linear model for stability analysis and fully nonlinear and three-dimensional for simulations), we incorporate finite walls to replace the isothermal boundary condition. A finite-wall model is studied by Howle [9]. In the parameter region studied the closed-loop behavior has an interesting oscillatory mode. As for our LQG compensator model, both the idealized and finite-wall versions are used. To avoid confusion, we denote the compensator with idealized boundary condi-

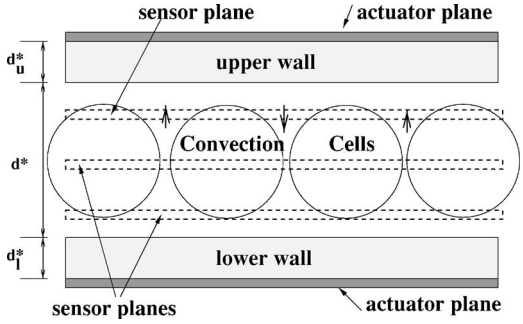

FIG. 1. The sensor and actuator location in the fluid layer.

tions [5] as C1 and the compensator with finite conductive walls as C3. Also, in addition to using one actuator plane at the bottom wall (referred as a single-plane actuator), an additional actuator plane at the upper wall (referred as a double-plane actuator) is used. For the evaluation of controller robustness, in our previous study [5], the plant, like the compensator, is set at the nominal parameters.

In Ref. [5], the Nyquist criterion provides the indicator for robustness. The Nyquist criterion gives the total margin. Moreover, no detailed investigation of the stability margin as a function of the wave number is provided. In this study, effects that impact robustness will be sorted out individually, as a function of wave number. The stability margins are obtained with respect to the Rayleigh number, actuator lag, sensor-plane depth uncertainty, wall thickness uncertainty, and single-plane versus double-plane actuators. Besides computing the stability limiting curves based on linear models, we also introduce a singular-value bound as a more conservative criterion for robustness, which is applicable to multi-input-multi-output (MIMO) plant systems. Besides the linear stability, we also investigate robustness using a fully nonlinear, three-dimensional (3D) simulation tool.

II. MATHEMATICAL FORMULATION

A. Plant model

In Fig. 1 we show a schematic of a section of an infinite layer of fluid, bounded by two finite-conductive walls with finite thickness. The fluid layer has thickness d^* [in this paper an asterisk denotes dimensional variables or compensator parameters (at nominal conditions)]. The outer surfaces of the lower and upper walls are prescribed at temperatures T_2^* and T_1^*, respectively. The upper and lower wall of thicknesses are d_u^* and d_ℓ^*. For nondimensional scalings we use the external temperature difference $\Delta T^* = T_2^* - T_1^*$ as the temperature scale and the fluid layer thickness d^* as the length scale. In addition, the fluid thermal diffusive time scale d^{*2}/κ^* is used for scaling time, where κ^* is the fluid's thermal diffusivity. The equilibrium conductive temperature modified by the presence of the finite walls is derived in the Appendix. In the nondimensional form, the fluid is governed by the Oberbeck-Boussinesq (OB) equations,

$$\mathrm{Pr}^{-1}\partial_t \mathbf{v} = \mathrm{Pr}^{-1}\mathbf{v} \times \boldsymbol{\omega} + \mathbf{k}\mathrm{Ra}\theta - \boldsymbol{\nabla}\pi_e + \boldsymbol{\nabla}^2\mathbf{v}, \tag{1}$$

$$\partial_t \theta = -\mathbf{v}\cdot\boldsymbol{\nabla}\theta + w + \boldsymbol{\nabla}^2\theta, \tag{2}$$

$$\boldsymbol{\nabla}\cdot\mathbf{v} = 0, \tag{3}$$

where $\mathbf{v}=(u,v,w)$ is the velocity vector field, $\omega=\boldsymbol{\nabla}\times\mathbf{v}$ is the vorticity, $\pi_e=\pi+\mathbf{v}\cdot\mathbf{v}/2$ is the effective pressure head, θ is the perturbation temperature with respect to the equilibrium conductive state. The z direction is directed upward and $\mathbf{k}$ is the unit vector.

The plant system has two external nondimensional parameters: the Rayleigh number and the Prandtl number. The Prandtl number is $\mathrm{Pr}=\nu^*/\kappa^*$, where ν^* is the kinematic viscosity. The Rayleigh number is defined in terms of the outer-wall temperature difference and the fluid layer thickness, $\mathrm{Ra}=\alpha^* g \Delta T^* (d^*)^3/\nu^*\kappa^*$, where α^* is the coefficient of thermal expansion. All the material properties are assumed constant. Note that Ra here is defined based on the outer wall-to-wall temperatures ΔT^* but fluid thickness d^*. The effective Ra_f should be defined based on the fluid boundary temperatures. In the Appendix, Ra_f is derived from Ra, by replacing d^* with d^*h, where h is a nondimensional factor. Equation (3) is the continuity equation for incompressible flow.

In addition to the OB equations describing the fluid layer, the lower and upper wall walls are governed only by the heat-transfer equations,

$$\partial_t \theta_\ell = \kappa_\ell \boldsymbol{\nabla}^2 \theta_\ell, \tag{4}$$

and

$$\partial_t \theta_u = \kappa_u \boldsymbol{\nabla}^2 \theta_u, \tag{5}$$

where $\kappa_\ell = \kappa_\ell^*/\kappa^*$ and $\kappa_u = \kappa_u^*/\kappa^*$.

The kinematic boundary conditions applied to the velocity field in the fluid layer, which are defined as the nonpermeable and nonslip conditions,

$$\mathbf{v}(x,y,0,t) = \mathbf{0}, \quad \mathbf{v}(x,y,1,t) = \mathbf{0}. \tag{6}$$

The fluid-wall interfacial thermal boundary conditions are dynamic, not prescribed. They are matched conditions of temperatures and heat flux,

$$\theta(x,y,0,t) = \theta_\ell(x,y,0,t),$$

$$\partial_z \theta(x,y,z,t)|_{z=0} = k_\ell \partial_z \theta_\ell(x,y,z,t)|_{z=0} \tag{7}$$

and

$$\theta(x,y,1,t) = \theta_u(x,y,1,t),$$

$$\partial_z \theta(x,y,z,t)|_{z=1} = k_u \partial_z \theta_u(x,y,z,t)|_{z=1}. \tag{8}$$

The parameters k_ℓ and k_u are the thermal conductivity ratios of the upper and lower wall materials defined in the Appendix, respectively.

The thermal actuators correspond to the prescribed outer wall thermal boundary conditions,

$$\theta_\ell(x,y,-d_\ell,t) = u_\ell(x,y,t), \tag{9}$$

where $u_\ell(x,y,t)$ is the temperature control input imposed at lower wall, and

$$\theta_u(x,y,1+d_u,t) = u_u(x,y,t), \tag{10}$$

where $u_u(x,y,t)$ is the temperature control input imposed at upper wall in case of two actuator planes. The control inputs to the plant u_ℓ and u_u are functions of the sensor outputs from the plant. Like in Ref. [5], we consider three sensor planes, located at $z=z_{sk}$, $k=1,2,3$. The sensor planes measure temperatures

$$z_{sk}(x,y,t) = \theta(x,y,z_{sk},t), \quad k=1,2,3. \tag{11}$$

The spectral decomposition of the three-dimensional velocity and temperature field variables and the fractional step, time-splitting method for integrating the fully nonlinear OB system of equations are described in detail in Ref. [6]. Details are provided in the references therein, in particular, by Marcus [7]. Here, only the addition of the conductive walls into the existing numerical scheme, described by Eqs. (4) and (5), will be mentioned with no repetitions.

Unfortunately, a direct incorporation of Eqs. (4) and (5) using the existing fractional-step approach [6] is numerically unstable. So, the three heat equations have to be solved simultaneously. Referring to Ref. [6], we add to the physical dependent variables two thermal fields (θ_ℓ, θ_u), besides the existing fields (u,v,w,p,θ). All the fields have independent variables (x,y,z,t), where each field has the same (x,y) coordinate ranges, but θ_ℓ, θ, and θ_u have different z coordinate ranges. We use three column vectors to represent the corresponding Fourier-Chebyshev coefficients $(\boldsymbol{\theta}_\ell, \boldsymbol{\theta}, \boldsymbol{\theta}_u)$ corresponding to the physical field variables $(\theta_\ell, \theta, \theta_u)$.

The finite wall temperature distribution has a simple closed-form solution if the diffusive term in the diffusive equations dominates and the time derivative term is negligible [10]. In general, a numerical solution is computed. At the nth time step (not fractional step), the wall temperatures are expressed as

$$\boldsymbol{\theta}_\ell^{(n+1)} = \mathbf{b}_1(\boldsymbol{\alpha}^T\boldsymbol{\theta}^{(n)}) + \mathbf{b}_2 u_\ell^{(n)}, \quad \boldsymbol{\alpha} = [1,-1,1,-1,\ldots]^T,$$

$$\boldsymbol{\theta}_u^{(n+1)} = \mathbf{b}_3(\boldsymbol{\beta}^T\boldsymbol{\theta}^{(n)}) + \mathbf{b}_4 u_u^{(n)}, \quad \boldsymbol{\beta} = [1,1,1,1,\ldots]^T, \tag{12}$$

where $\boldsymbol{b}_j$ $(j=1,4)$ are obtained by inverting the two matrix equations for the wall heat equations. The implicit Euler and tau method are used here. For the lower wall heat equation, its lower boundary condition is the lower wall control and its upper boundary condition can be either the interfacial temperature matching condition or the interfacial heat flux matching condition. Similar conditions for the boundary conditions of the upper wall heat equation are developed, although we choose the interfacial temperature matching conditions as the boundary conditions for solving the wall heat equations. The two scalar controls, u_ℓ and u_u are either functions of (x,y,t) (in physical space) or (k_x,k_y,t) (in Fourier space). In this way, the wall temperatures are explicitly solved in terms of the two control parameters and the fluid layer temperature distribution.

We can now replace the idealized lower and upper boundary conditions [i.e., $\theta(x,y,0,t)=u_\ell(x,y,t)$ and $\theta(x,y,1,t)=u_u(x,y,t)$] previously used [6] by the following conditions, respectively:

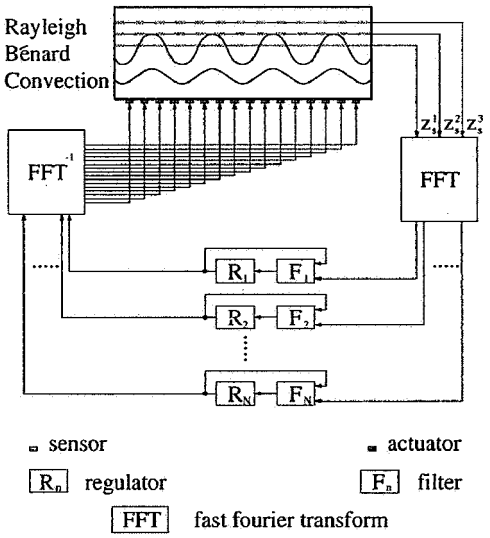

FIG. 2. The LQG control loop diagram.

$$\left(\boldsymbol{\alpha}^T\mathbf{D} - \frac{k_\ell}{d_\ell}(\boldsymbol{\beta}^T\mathbf{D}\mathbf{b}_1)\boldsymbol{\alpha}\right)\boldsymbol{\theta}^{(n+1)} = \frac{k_\ell}{d_\ell}(\boldsymbol{\beta}^T\mathbf{D}\mathbf{b}_2)u_\ell^{(n)},$$

$$\left(\boldsymbol{\beta}^T\mathbf{D} - \frac{k_\ell}{d_\ell}(\boldsymbol{\alpha}^T\mathbf{D}\mathbf{b}_3)\boldsymbol{\beta}\right)\boldsymbol{\theta}^{(n+1)} = \frac{k_\ell}{d_\ell}(\boldsymbol{\alpha}^T\mathbf{D}\mathbf{b}_4)u_u^{(n)}, \tag{13}$$

where $\mathbf{D}$ is the first derivative matrix defined for $z=0,1$ for the Chebyshev coefficients ($\theta \to \partial_z\theta$ corresponds to $\boldsymbol{\theta} \to \mathbf{D}\boldsymbol{\theta}$). If the interfacial temperature matching conditions are used for the wall temperatures, then the interfacial heat flux matching conditions have to be used for the fluid, and vice versa. It can be shown that, as $k_\ell/d_\ell \to \infty$, the lower wall boundary condition approaches the idealized boundary condition used in our previous studies. A similar condition holds for the upper wall boundary condition. An actuator lag for the controls is incorporated as an additional plant state.

B. Modally distributed LQG compensator

The LQG compensator design is described in detail in Ref. [5]. We will not repeat the details here. In brief, each compensator (denoted as a transfer function matrix $\mathbf{K}_{mn}$ below, $m=1,2,\ldots,N_x$, $n=1,2,\ldots,N_y$, see Fig. 2), is of the linear quadratic Gaussian and loop transfer recovery (LQG-LTR) type. The LTR approximation provides almost the full-state feedback performance of ±60° phase margin and −6 dB to ∞ in lower and upper gain margins, by allowing the observer weighting parameter $\beta \to \infty$ [11]. As in our previous design [6], we use $\beta=10^3$. We use the regulator weighting parameter $\gamma=0.1$. Note that $\gamma \to 0$ corresponds to unlimited control authority. In addition to the compensator parameters γ and β, the compensator has system model that involves the major physical parameters of the problem; the Rayleigh number as Ra^* and the wave number as (mk_x^*, nk_y^*) (the asterisk denotes nominal values). When the nonlinear plant yields a solution described by a 2D wave number array (mk_x, nk_y) for $m=1,2,\ldots,N_x$, and $n=1,2,\ldots,N_y$, then the compensator consists of $N=N_xN_y$ single-wave-number sub-

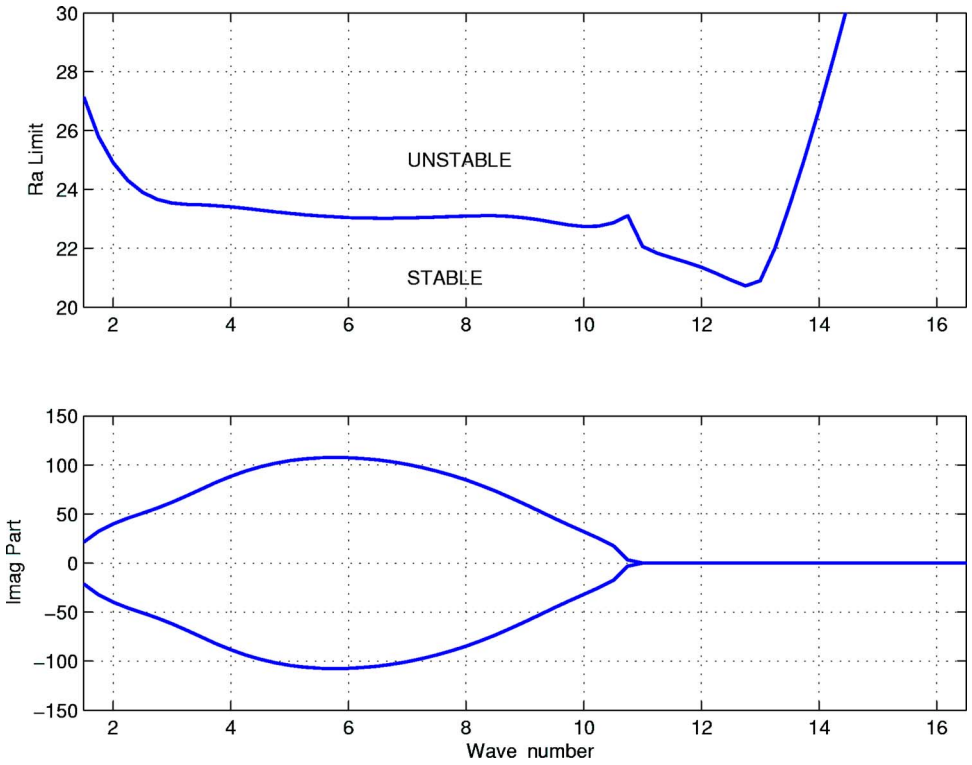

FIG. 3. (Color online) Stability margin in Ra vs k for Pr=7.0 (upper panel) and corresponding imaginary eigenvalue (lower panel).

compensators. A kth subcompensator consists of a Kalman filter F_k and a optimal regulator R_k ($k=1,2,\ldots,N$). The three levels of temperatures in Fig. 2 are denoted by Z_1, Z_2, and Z_3. The output from the kth compensator is either one or two scalar controls, depending on one or two actuator planes used. The corresponding plant parameters (without asterisk, with uncertainties) can differ from the compensator parameters (with asterisk, at nominal conditions). Figure 2 presents a block diagram showing the Fourier-decomposed nonlinear plant. All inputs and outputs are Fourier-Chebyshev coefficients. Each Fourier mode disturbance corresponding to wave numbers (mk_x, nk_y) is controlled by a LQG compensator $\mathbf{K}_{mn}$ designed at the nominal wave numbers (mk_x^*, nk_y^*). The greater the difference between the compensator and plant parameters while preserving closed-loop stability, the more robust the compensator, i.e, the greater the stability margins. We denote the compensator corresponding to idealized thermal boundary condition as C1, and the one incorporating finite walls as C3. The reduced-order compensator [8] is used here. Since our focus is on robustness, we will not deal with the transient conductive state nor will the gain-scheduling algorithm be used.

III. RESULTS

A. Linear stability using a single-plane actuator

In the linear stability study, a linearized plant dynamical model is used. We assume the material properties of the upper and lower walls to be the same, corresponding to aluminum at room temperature. The walls have thickness 1/10 of the fluid depth. For the working fluid using water we have Pr=7.0, $K_l=K_u=400$, and $\kappa_l=\kappa_u=670$. Using air we have Pr=0.7, $K_l=K_u=8800$, and $\kappa_l=\kappa_u=4.2$ instead.

1. Major parameter uncertainties

Our nominal model consists of one actuator, located at outer surface of the lower wall, at $z=-d_l$ and three sensor planes, located at $z_{s1}=0.2$, $z_{s2}=0.5$, and $z_{s3}=0.8$. These are optimal sensor locations according to our previous analysis [5]. The nominal $\mathrm{Ra}^*=20\,\mathrm{Ra}_c$, where $\mathrm{Ra}_c\approx 1707.762$ is the critical Rayleigh number. The LQG compensator is designed at the nominal values (denoted by an asterisk). In the nonlinear simulations [6–8] the compensator consists of an array of single-k controllers. The nominal wave number k^* is an array evenly spaced wave numbers covering the entire unstable band at Ra^*. In the linear stability analysis, the nominal wave number k^* is a prescribed parameter that can be varied across the unstable band. Here the compensator is assumed to be designed at (k^*, Ra^*). At nominal condition, the plant model has $k=k^*$ and $\mathrm{Ra}=\mathrm{Ra}^*$. For robustness investigation, we vary k and Ra from their nominal values.

The eigenvalue analysis indicates that the closed-loop system using the steady-state LQG compensator is always stable at the nominal condition, i.e., at $k=k^*$ and $\mathrm{Ra}=\mathrm{Ra}^*$ even when Ra^* is as large as $100\mathrm{Ra}_c$. However, at high Ra exceeding, say, $20\mathrm{Ra}_c$, the least stable eigenvalue becomes sensitive to small changes in the prescribed parameter. This is an indication of weakening of robustness at large Ra.

In the following, we vary the plant parameter Ra from the nominal value $\mathrm{Ra}^*=20\mathrm{Ra}_c$ to see how far the system can tolerate the change before becoming unstable. The result presents the stability margin $\Delta\mathrm{Ra}=\mathrm{Ra}-\mathrm{Ra}^*$ in terms of the wave number k^*. In doing so we assume that the plant wave number k is unchanged from the nominal value k^*. In Figs. 3 and 4, we show the results Ra vs k for the case at Pr=7.0 and Pr=0.7, respectively. The margin ΔRa is the range above 20. For the two values of Pr, the results appear very similar. The

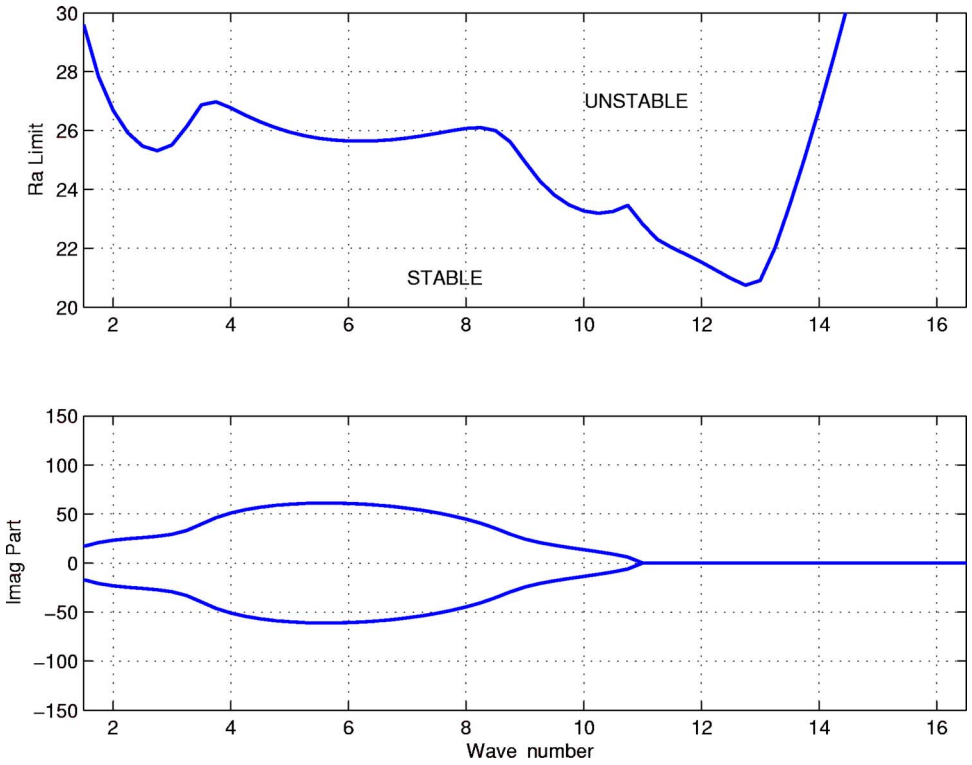

FIG. 4. (Color online) Stability margin in Ra vs k for Pr=0.7 (upper panel) and corresponding imaginary eigenvalue (lower panel).

margin in Ra (upper panels) dips to a minimum near $k=13$. Although the minimal margin occurs at approximately four times the critical wave number $k_c \approx 3.117$, in the nonlinear simulations presented later, we see no sign that short-wave modes are being excited. In fact, nonlinearity is stabilizing by cascading disturbances to shorter and shorter harmonic modes that promote diffusions. Beyond $k=13$, the modal diffusive terms become very large and stabilizing; the Ra margin is expected to increase unboundedly. The pair of imaginary eigenvalues with zero real part is shown in the lower panels. The result shows that, for positive plant uncertainty in Ra (i.e., $\mathrm{Ra} > \mathrm{Ra}^*$), the closed-loop behavior first becomes unstable to an oscillatory mode at lower wave number and to a monotonic mode at higher wave number. For negative plant uncertainty in Ra (i.e., $\mathrm{Ra} < \mathrm{Ra}^*$), the closed-loop behavior is always stable.

We turn to the wave number margins. Here we assume there is no uncertainty in Ra, i.e., $\mathrm{Ra}=\mathrm{Ra}^*=20\mathrm{Ra}_c$. We vary the nominal wave number k^* and at each value of k^* we determine the Δk margins, $\Delta k = k - k^*$, where there are two values of Δk, the upper and lower Δk stability limit. Again, we consider the cases of Pr=7.0 (Fig. 5) and Pr=0.7 (Fig. 6). Again, we see that the behavior for both cases are very similar. In both cases, the upper Δk margin (upper curve) increases steeply beyond $k^*=8$. The lower k margin (lower curve) behaves in a rather complicated fashion. The margin diverges between $k^*=4.0$ and 5.0 but between $k^*=5.0$ and the Δk minimum near $k^*=13$, the margin is quite flat. Then, beyond $k^*=13$, the lower Δk margin increases linearly. It appears that the stability margin is weakest near $k^*=13$, which means that the closed-loop system is least robust with respect to, or most vulnerable to, unstable mode onset for a spatial length scale corresponding to $k^*=13$, or a wavelength $\lambda^* = 2\pi/k^*$, approximately 1/2 of the layer depth.

We emphasize that the three-level sensor configuration is important for robustness. Decreasing the number of sensor planes or moving the outer sensor planes towards the wall will erode the state observability. As a result, closed-loop stability is only achievable at much lower Ra^*.

2. Actuator lag

A potential destabilizing effect arises from the actuator lag. Both finite conductivity and electronic processing in the thermal actuator contribute to the actuator lag. A first-order lag effect is incorporated in the linearized plant model and later in the nonlinear plant, described by the transfer function (TF) $G_d = \omega_d/(s+\omega_d)$ where s is the Laplace-transformed value. This TF has to be modeled in between the compensator output u_o and the plant input u_i. Because of the lag, we have

$$\dot{u}_i + \omega_d u_i = \omega_d u_o. \tag{14}$$

For large ω_d, or small lag time constant $\tau_d = 2\pi/\omega_d$, the effect is small, i.e., $u_o \approx u_i$. But for large τ_d, the lag can be destabilizing. To model the actuator lag, we write the linear plant state-space equation as $\dot{\mathbf{x}} = \mathbf{A}\mathbf{x} + \mathbf{B}u_i$, where u_i is given in Eq. (14). The compensator output u_o can be used as the input to the plant model, modified as

$$\begin{bmatrix} \dot{\mathbf{x}} \\ \dot{u}_i \end{bmatrix} = \begin{bmatrix} \mathbf{A} & \mathbf{B} \\ \mathbf{0} & -\omega_d \end{bmatrix} \begin{bmatrix} \mathbf{x} \\ u_i \end{bmatrix} + \begin{bmatrix} \mathbf{0} \\ \omega_d \end{bmatrix} u_o,$$

$$\mathbf{y} = [\mathbf{C} \quad 0] \begin{bmatrix} \mathbf{x} \\ u_i \end{bmatrix}. \tag{15}$$

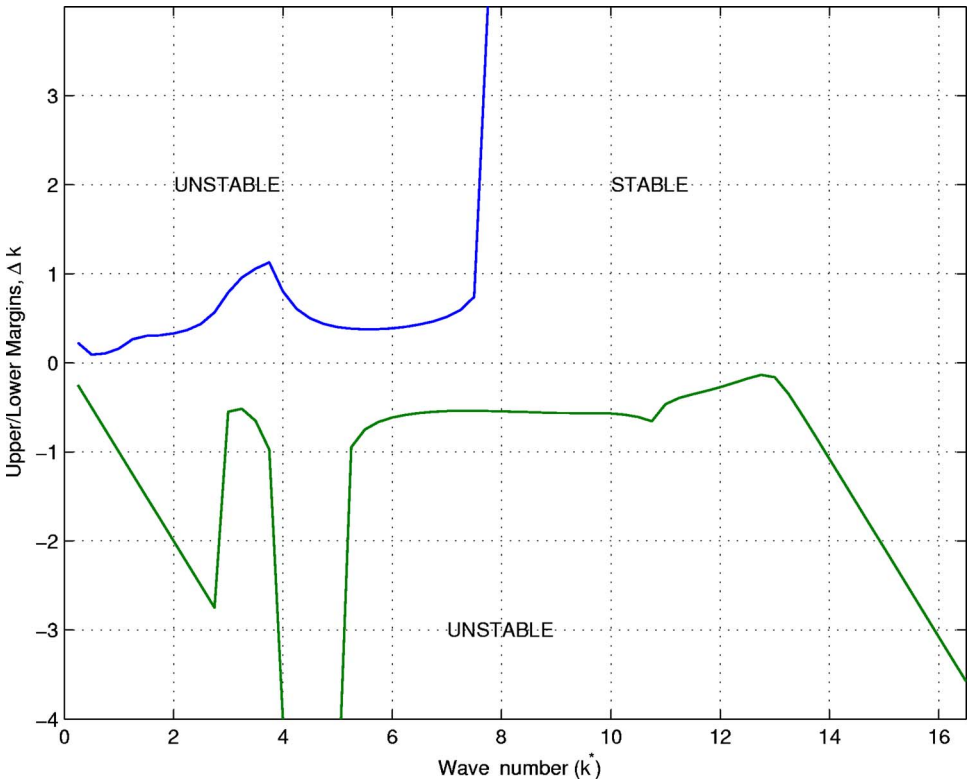

FIG. 5. (Color online) Margins Δk vs k^* for $\mathrm{Ra}=20\mathrm{Ra}_c$, Pr=7.0.

In Fig. 7, we show the destabilizing effect of the actuator lag by plotting the real part of the least stable eigenvalue (growth rate) versus wave number. In this case, both plant and compensator parameters are set to the same condition, with $k=k^*$, $\mathrm{Ra}=\mathrm{Ra}^*=20\mathrm{Ra}_c$. The left panel shows the case for Pr=7.0 and the right panel shows the case for Pr=0.7. In both cases, the least-stable eigenvalue (real) is shown as a function of the wave number (k) for three lag time constants, $\tau_d=0.001$, 0.003, and 0.005. These are in nondimensional time unit. In the wave-number band between $k=3$ and $k=8$ for the case of Pr=7.0, a sufficiently large lag time-constant causes instability. For the case Pr=0.7, however, the lag has

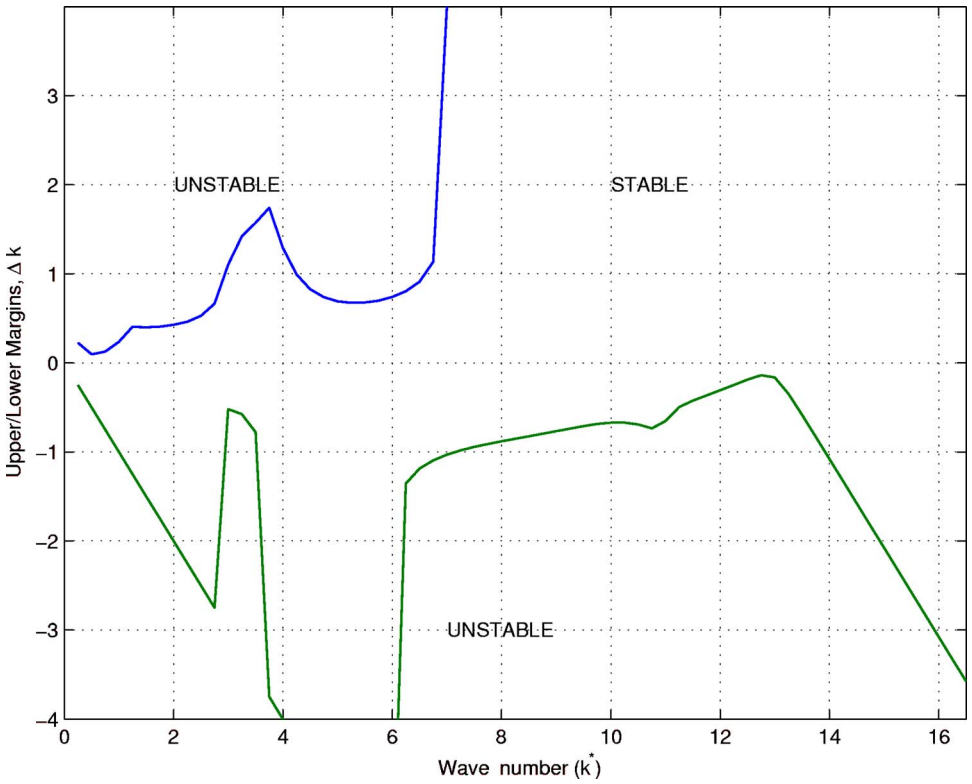

FIG. 6. (Color online) Margins Δk vs k^* for $\mathrm{Ra}=20\mathrm{Ra}_c$, Pr=0.7.

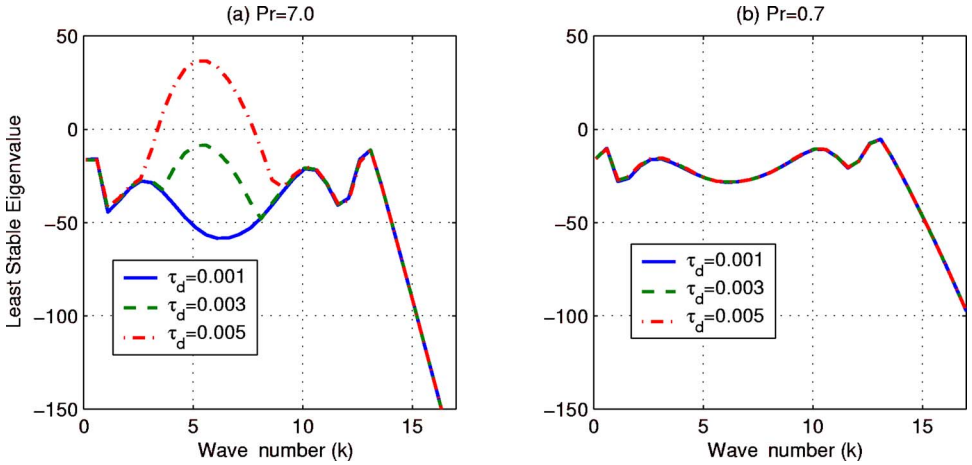

FIG. 7. (Color online) Least stable eigenvalue vs k with actuator lag.

no destabilizing effect. For the case Pr=0.7, τ_d=0.003 almost drives the Fourier mode at k=5 unstable. For the case Pr=0.7, the actuator lag is more destabilizing for higher wave number. The eigenvalue peaks near k=13.

The nondimensional time scale is d^2/κ. For water and layer thickness d=0.5 cm, one nondimensional time unit =176 s at standard temperature pressure (STP). For air κ is about 145 times that of water. In order to get the same nondimensional time scale d for air has to be 12 times that of d for water. For the nondimensional time scale, if the layer thickness is 0.5 cm, say for water at STP, a physical lag τ_d =0.001 corresponds to 0.18 s, roughly; and that for air is only 0.001 s. One can always stretch the physical lag time for the same value of τ_d, by increasing the layer depth of air. In order to maintain the same Ra for air (Ra is proportional to d^3/κ for a given temperature difference), however, this implies decreasing the temperature difference for air.

3. Sensor plane depth uncertainty

The sensor-plane depth uncertainty turns out to be a difficult problem. The nominal sensor plane depths are z_1^*=0.2, z_2^*=0.5, and z_3^*=0.8 (scaled by the fluid layer thickness). Consider the compensator model to have these nominal values but the plant model has corresponding plane depths of $z_1=z_1^*+\Delta z_1$, $z_2=z_2^*+\Delta z_2$, and $z_3=z_3^*+\Delta z_3$ where the perturbations are due to uncertainties. We assume each of Δz_i is a zero-mean Gaussian number with standard deviation 0.01. Consider the case Pr=7.0, Ra=Ra*=2000, $k=k^*$=3.5. We use the C3 compensator for the three-layer plant model. Figure 8 shows the results for 5000 Monte Carlo runs. For each realization of error $(\Delta z_1, \Delta z_2, \Delta z_3)$, the closed-loop, least stable eigenvalue is computed. If the real part is less than or equal to zero, a dot is shown in the plot. The ensemble shows where the stable region lies on the 3D error space. Panels

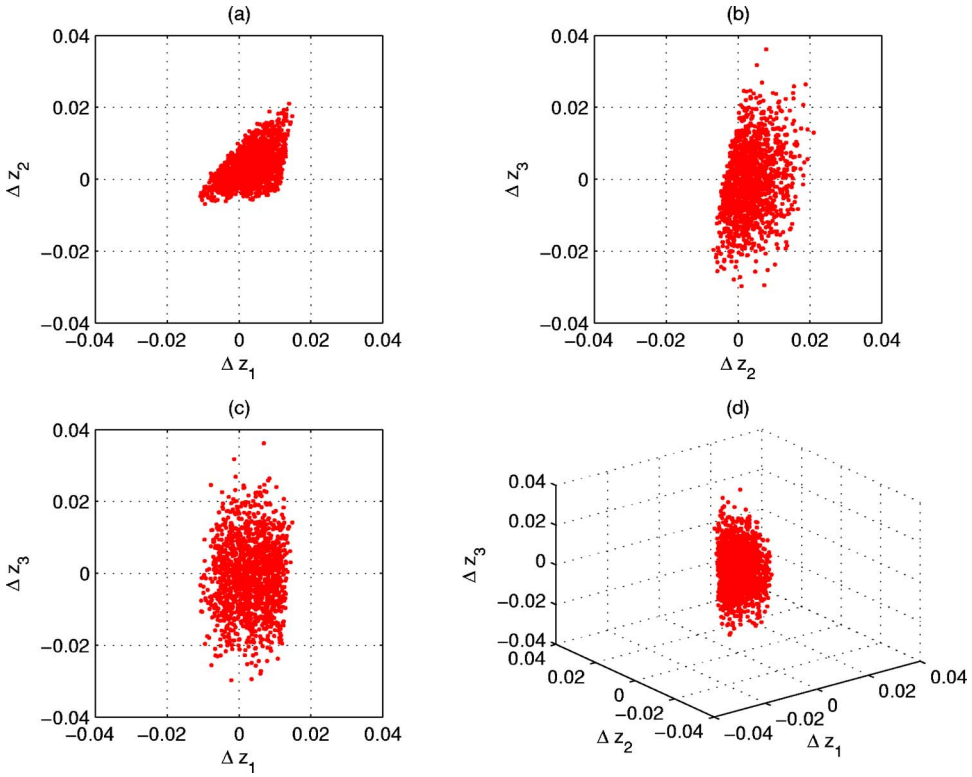

FIG. 8. (Color online) Stable region in the 3D error space from 5000 Monte Carlo runs.

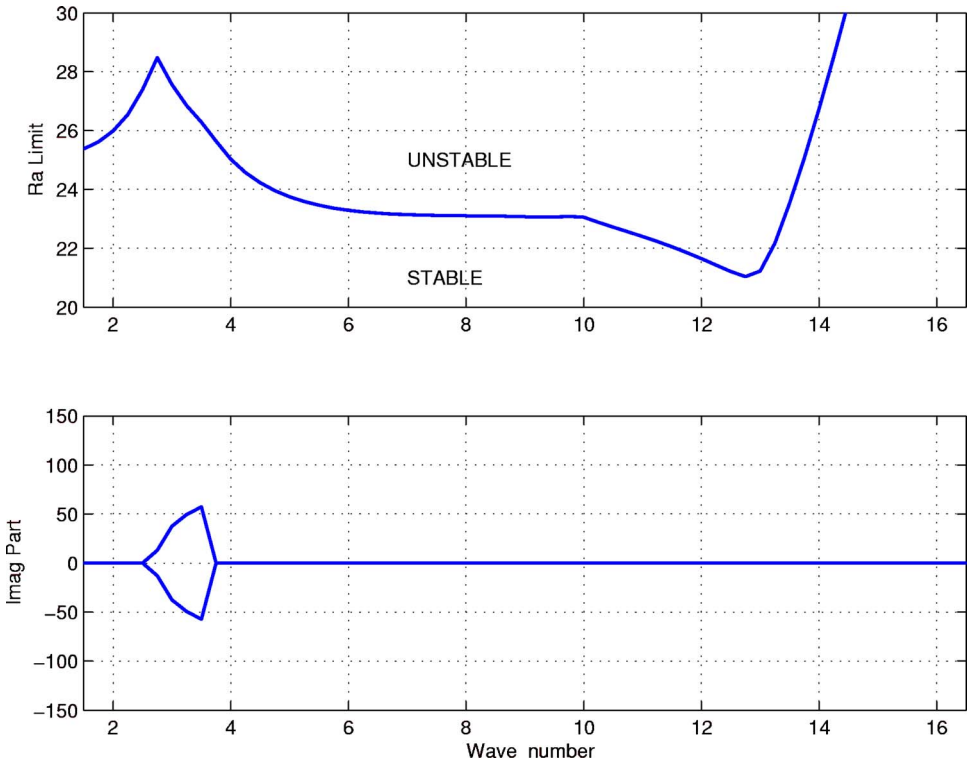

FIG. 9. (Color online) Stability margin in Ra vs k for Pr=7.0 (upper panel), and corresponding imaginary eigenvalue (lower panel).

(a)–(c) are projection of the points (stable) onto the Δz_1 vs Δz_2 plane, Δz_2 vs Δz_3 plane, and Δz_1 vs Δz_3 plane, respectively. The last panel shows the 3D plot of the points. The unstable points are not shown. The figures use a uniform scale per axis from −0.04 to 0.04. The results indicate that (i) the stable region in the 3D error space is quite small; (ii) Δz_3 appears to be the least significant error among the three, relatively speaking. It means the sensor plane farthest from the actuator plane can tolerate largest uncertainty; (iii) both Δz_1 and Δz_2 are important. However, the shape of the stable region is not symmetric with respect to the sign of error. It appears less destabilizing if the first and second sensor planes are moving away from the actuator, more destabilizing if both are moving towards the actuator. It is worse if one is moving away but the other is moving towards the actuator. The sensor-plane depth errors can be a significant challenge in the laboratory implementation.

B. Linear stability using two actuator planes

It is of interest to see if there will be improvement in the robustness by the addition of an extra actuator plane on the outer face of the upper wall. This addition makes the plant a three-input-two-output system. We choose to show the case Pr=7.0 only. In Fig. 9, we show the Ra margin in k as in the nominal case. The margin curves are very similar to the ones before. Only a very slight improvement in margins is evident. The improvement is not significant. Compared the second panel between Figs. 3 and 9, the k band for imaginary part of the least-stable eigenvalue becomes significantly smaller. In Fig. 10, we show the upper and lower k margins vs k. Again, the improvement with an additional actuator is small.

1. Singular-value bounds

Doyle and Stein [11] develop an approach to use the singular values bounds for relative stability measure in finite-dimensional, linear-time-invariant (FDLT) systems. The conditions give bounds that guarantee stability but these are not necessarily tight bounds, therefore, more conservative. To illustrate the idea, it is more convenient to use the transfer function (TF) notation. The TF between input and output of the state-space system $(\mathbf{A},\mathbf{B},\mathbf{C},\mathbf{D})$, corresponding to the standard dynamical and output equations $\dot{\mathbf{x}}=\mathbf{A}\mathbf{x}+\mathbf{B}\mathbf{u}$ and $\mathbf{y}=\mathbf{C}\mathbf{x}+\mathbf{D}\mathbf{u}$ (after Laplace transform) is $\mathbf{y}(s)=\mathbf{G}(s)\mathbf{u}(s)$, where $\mathbf{G}(s)=\mathbf{C}(s\mathbf{I}-\mathbf{A})^{-1}\mathbf{B}+\mathbf{D}$. Here, we use $\mathbf{G}(s)$ to denote the plant TF. In the following, both plant and compensator TFs correspond to a single-wave-number model. There are two common ways to model uncertainties. One is by additive perturbation to the nominal $\mathbf{G}(s)$, $\mathbf{G}'=\mathbf{G}+\Delta\mathbf{G}$. The other is by multiplicative perturbation to the nominal $\mathbf{G}(s)$, $\mathbf{G}'=(\mathbf{I}+\mathbf{L})\mathbf{G}$, where $\mathbf{L}$ is a multiplicative error model derived based on $\mathbf{G}'$ and $\mathbf{G}$. Here, the latter way is adopted. To keep the uncertainties within bounds, we require $\bar{\sigma}(\mathbf{L})<\ell_m(\omega)$ for some prescribed function of frequency, $\ell_m(\omega)$. Here $\bar{\sigma}$ and $\underline{\sigma}$ denote the upper and lower bound singular values, respectively. The LQG compensator, denoted by $\mathbf{K}(s)$ is defined by state space system $((\mathbf{A}^*-\mathbf{K}_f\mathbf{C}^*-\mathbf{B}^*\mathbf{K}_c),\mathbf{K}_f,-\mathbf{K}_c\mathbf{D}^*)$, where $\mathbf{K}_f$ and $\mathbf{K}_c$ are the filter and regulator gains, respectively. Otherwise, the matrices are identical to those of the linearized plant.

There are two ways consider breaking the loop of a compensated plant. One is by breaking the loop at the plant output [see Fig. 11(a)]. This case gives a compensated plant TF equal to $\mathbf{GK}(s)$ and the other is by breaking the loop at the plant input [see Fig. 11(b)]. In both figures, the dashed line in

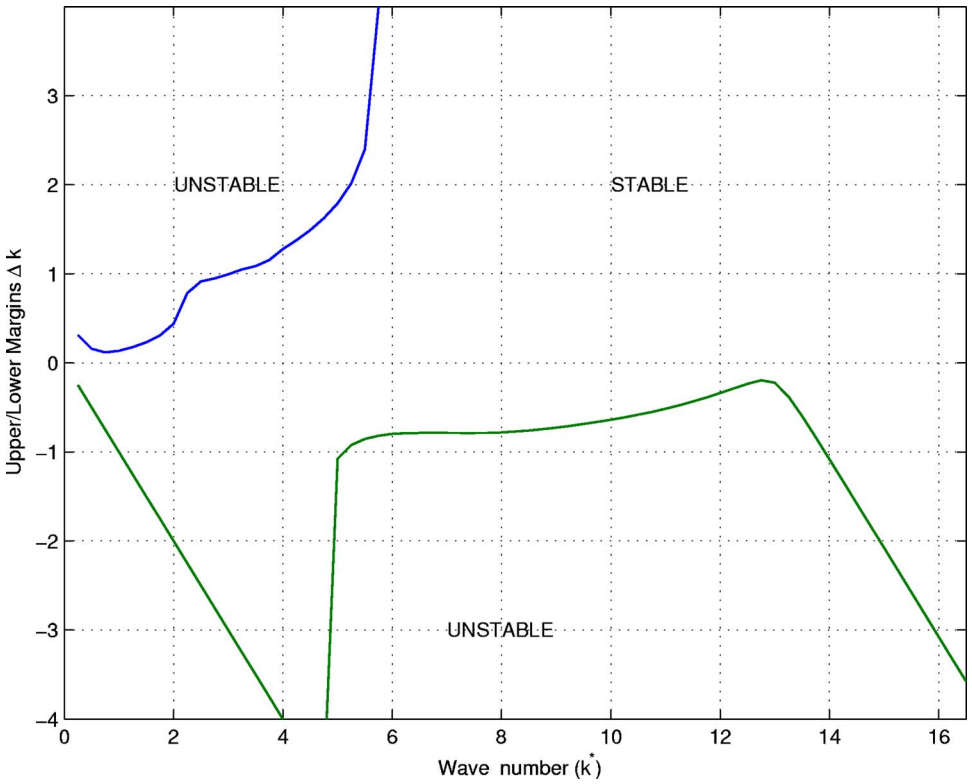

FIG. 10. (Color online) Margins Δk vs k^* for $\mathrm{Ra}=20\mathrm{Ra}_c$, $\mathrm{Pr}=7.0$.

the loop denote the broken loop. This case gives a compensator plant TF of $\mathbf{KG}(s)$ (note that the matrix columns correspond to the inputs and matrix rows correspond to the outputs). In Ref. [5], we considered a plant with one actuator plane (one input) and three sensor planes (three outputs). Therefore the dimensions of $\mathbf{G}(s)$ is 3×1. The compensator takes the three plant outputs as measurements to produce one control therefore the dimension of $\mathbf{K}(s)$ is 1×3. The advantage by breaking the loop at the plant input is that we obtain a single-input-single-output (SISO) $\mathbf{GK}(s)$. Therefore, as demonstrated in Ref. [5], the relative stability can be effectively analyzed using gain and phase margins, based on the classical Nyquist criterion.

Here, the Doyle and Stein condition provides an independent means to assess the stability margins, apart from the parameter margin curves from the direct closed-loop computation. We consider two actuator planes and three sensor planes. The Nyquist criterion can no longer be applied. Consider breaking the loop at the plant output (the argument is equally valid for breaking the loop at the plant input. In the present case, however, the plant has two plant inputs versus three outputs, we caution that the 3×3 matrix $\mathbf{GK}$ is rank deficient by 1). Doyle and Stein [11] noticed that to guarantee stability in the presence of uncertainties, $\mathbf{G}'\mathbf{K}(s)$ has to preserve the system dimensions of $\mathbf{GK}(s)$. If the compensated plant has equal inputs and outputs, then the generalized Nyquist criterion on the determinant is that the number of encirclement of $\det(\mathbf{I}+\mathbf{G}'\mathbf{K})$ remains unchanged from $\det(\mathbf{I}+\mathbf{GK})$. Preserving the system dimensions means that the lower bound of the singular value of $\mathbf{I}+\mathbf{G}'\mathbf{K}$ is positive definite. That is,

$$0 < \underline{\sigma}[\mathbf{I}+(\mathbf{I}+\mathbf{L})\mathbf{GK}]. \tag{16}$$

Since $(\mathbf{I}+\mathbf{GK})$ is full rank, we pull it out as the common factor. Then, we require

$$0 < \underline{\sigma}[\mathbf{I}+\mathbf{LGK}(\mathbf{I}+\mathbf{GK})^{-1}] \tag{17}$$

for all ω and $\mathbf{L}$, or

$$\overline{\sigma}[\mathbf{GK}(\mathbf{I}+\mathbf{GK})^{-1}] < 1/\ell_m. \tag{18}$$

Using the matrix identity

$$\mathbf{GK}(\mathbf{I}+\mathbf{GK})^{-1} \equiv [\mathbf{I}+(\mathbf{GK})^{-1}]^{-1} \tag{19}$$

the stability condition according to Ref. [11] is

$$\overline{\sigma}[\mathbf{L}(\omega)] < \underline{\sigma}[\mathbf{I}+(\mathbf{GK})^{-1}], \tag{20}$$

where the right-hand term is referred to as the matrix return difference of the loop and $\ell_m(\omega)$ represents the singular-value bound of the error model $\overline{\sigma}(\mathbf{L}(\omega))$. Note that $\mathbf{GK}$ commutes with $(\mathbf{I}+\mathbf{GK})^{-1}$. In the following, we apply the Doyle-Stein's stability condition to investigate two separate

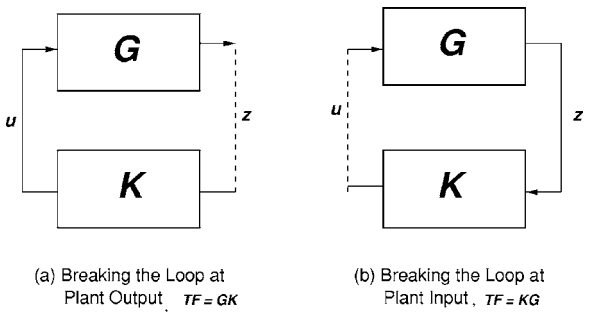

FIG. 11. Block diagram showing breaking the compensated plant loop.

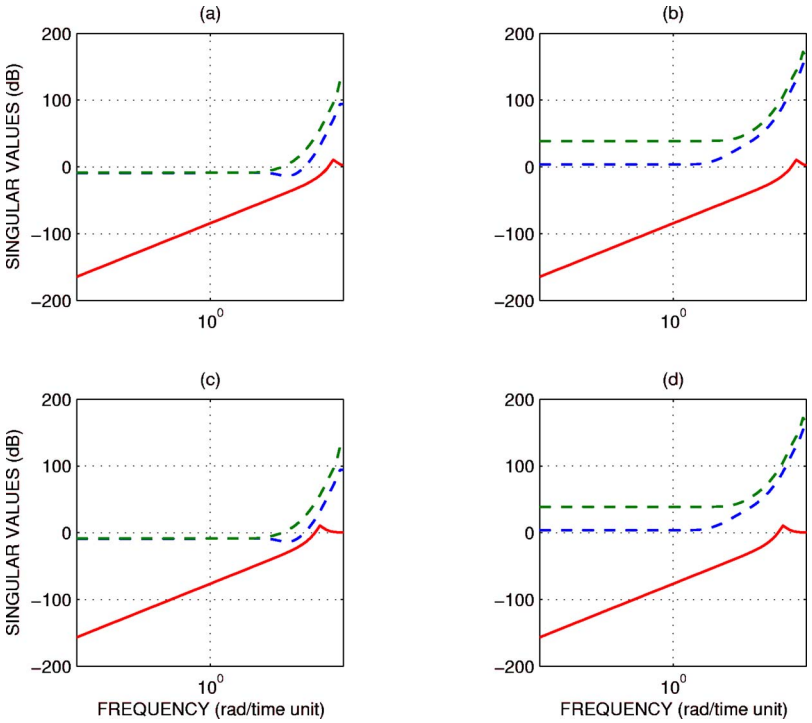

FIG. 12. (Color online) SinguIar-value bounds with the actuator error model.

problems. One is the actuator lag. The other is the finite wall thermal properties. The actuator is based on a second-order lag model according to Ref. [12]. Let L (for this case a scalar) be given by

$$\bar{\sigma}(L(\omega)) = \left| \frac{s^2 + 2\xi\omega_a s}{s^2 + 2\xi\omega_a s + \omega_a^2} \right| s = j\omega. \tag{21}$$

A damping factor $\xi=0.15$ is used but ξ is not a sensitive parameter. Decreasing ξ to 0.05 gives roughly the same results. In Figs. 12(a) and 12(b), we show the case $\omega_a=5000$ and in Figs. 12(c) and 12(d), we show $\omega_a=2000$. These are nondimensional frequencies. The corresponding physical frequencies are typically two orders of magnitude lower. The left panel corresponds to $k=6.5$ and the right panel to $k=13.0$. The higher wave-number system appears more robust with respect to the actuator lag than the lower wave number. In each panel the two dashed curves correspond to the lower-bound singular values [see the right-hand side of inequality (20)]. The solid curve shows $\bar{\sigma}(L)$. The stability margin corresponds to the gap between the lower dashed curve and the solid curve. The larger the gap, the greater the margin. The result appears fairly consistent with those of Fig. 7. The upper-bound singular value of the actuator lag is shown in the lowest curve in each panel of the figure. Now, the lag time constant is $\tau_a=2\pi/\omega_a$. The smaller ω_a the greater the lag and the more destabilizing the lag effect becomes. The closed-loop system remains stable. The physical implication is this. For water as fluid, an actuator lag time constant of 0.5 s will not trigger instability. For air at STP, this time constant is shortened by a factor of roughly 150 times. It appears that if the physical dimensions are unchanged, controlling convection in air requires a much higher-bandwidth controller than in water. Next, we address the problem of uncertainties of the finite wall thermal properties. Here, we construct a plant error model, denoted by $\Delta\mathbf{A}$ and $\Delta\mathbf{B}$ (where $\mathbf{C}$ and $\mathbf{D}$ are not affected) by the following. Let $\Delta\kappa_u=\Delta\kappa_\ell=\Delta\kappa$ and $\Delta K_u=\Delta K_\ell=\Delta K$. We compute the derivatives $\partial\mathbf{A}/\partial\kappa$, $\partial\mathbf{B}/\partial\kappa$, $\partial\mathbf{A}/\partial K$, and $\partial\mathbf{B}/\partial K$. So

$$\Delta\mathbf{A} = \frac{\partial\mathbf{A}}{\partial\kappa}\Delta\kappa + \frac{\partial\mathbf{A}}{\partial K}\Delta K,$$

$$\Delta\mathbf{B} = \frac{\partial\mathbf{B}}{\partial\kappa}\Delta\kappa + \frac{\partial\mathbf{B}}{\partial K}\Delta K. \tag{22}$$

Note that the error model affects only the plant and the compensator remains at nominal parameters. From the error model, it is somewhat tedious, but quite straight forward to generate the TF version of the error $\mathbf{L}$ by keeping the first-order error terms (the derivation will not be produced here). Figures 13(a) and 13(b) shows the singular-value bounds for the same wave numbers $k=6.5$ and 13.0, respectively. In this case, we let $\Delta\kappa$ and ΔK to be 25% of the nominal values. The dashed curves are the same as in Fig. 12. The pair of lower solid curves represent the two singular values of $\mathbf{L}(\omega)$. The solid and dashed curves very barely intersect for the $k=6.5$ case near $\omega\approx 700$. It appears that stability is preserved in the presence of 25% uncertainties in the wall thermal properties (both diffusivity and conductivity), about the nominal values.

C. 3D nonlinear closed-loop simulations

1. Model setup and assumptions

The compensator is linear, set at the nominal parameters and the plant model is 3D, nonlinear with uncertainties about the nominal parameters. The closed-loop system in the presence of uncertainties is investigated by examining the

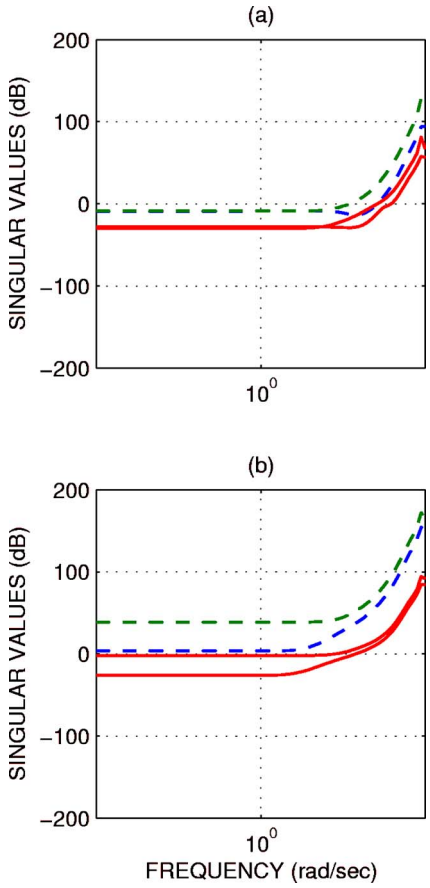

FIG. 13. (Color online) Singular-value bounds with the finite wall property error model.

closed-loop time response of the upper and lower-wall Nusselt numbers. Like in Refs. [6–8], the measure of the residual convection can be effectively shown using the Nusselt number plots. The Nusselt numbers at the upper and lower wall measure the ratios of total heat flux (convective and conductive) to the conductive heat flux leaving and entering the fluid layer. As Nusselt number approaches the value 1.0, the fluid layer convection is removed. Robustness is determined based on how much mismatches can be tolerated before the closed-loop system is unstable.

Although the parameter field is extremely vast, we have simulated a large number of cases but for limited space only a selective number of representative cases are presented. Since the focus of this paper is the robustness of the closed-loop system with respect to parameter mismatches, the Rayleigh number is set at a constant during the simulation. No gain-schedule algorithm [8] will be engaged. The nominal parameters are set at Pr=7.0, $\mathrm{Ra}^*=2\times10^4$, $k_x^*=k_y^*=1.0$. Unlike the linear analysis, these are fundamental wave numbers. The nominal geometric and material properties, sensor and actuator configurations are the same as in the linear analysis (see first paragraph of Sec. III A). The simulations correspond to 32×32 Fourier modes (horizontal). The integration and output sampled step is $\Delta t=0.004$. The simulation period T is 0.4 time units. Only one set of initial condition is used, corresponding to the residual state of the closed-loop simulation at $t=0.4$ presented in Ref. [8]. We use two versions of the LQG compensator, C1 and C3, designs based on a one-layer and three-layer model, respectively. Both are based on a reduced-order linear model consisting of only eight vertical complex modes (contrast to 64 vertical real modes in the plant model).

2. Finite wall properties

We selected a handful of cases to characterize the closed-loop behavior (both stable and unstable cases included). Figure 14(a) shows the upper and lower Nusselt number responses when the compensator C1 is used. The plant parameters are set at nominal. Note that the compensator has idealized thermal boundary conditions whereas the plant has finite walls incorporated. The upper (dashed) and lower Nusselt number (solid) show convection damped out in time. We then switch to compensator C3, the time response (not shown here) is visibly indistinguishable from that of Fig. 14(a).

Keeping the plant at nominal condition, now we reduce the upper and lower wall's thermal conductivity and diffusivity values each by 50%. The closed-loop system is stable with C1 as well as C3.

Next, we increase both wall thicknesses from the nominal value to $d_\ell=d_u=0.15$. Compensator C1 is not capable of suppressing convection any longer. Figure 14(b) shows the initial response. Eventually, the solution diverges. Using compensator C3, with the nominal wall thicknesses at 0.1, C3 still cannot damp out convection. In this case, the solution takes longer to diverge (plot not shown).

We conclude that the mismatches in wall thermal properties between the compensator and plant up to 50% is easily tolerated. But the mismatch in wall thickness is significantly more sensitive.

3. Simulations with actuator lag

In evaluating the actuator lag, we reset all the plant parameters to nominal values. To incorporate the first-order actuator lag, the last of Eqs. (15) has to be incorporated into the time-splitting algorithm of the 3D nonlinear plant model. We rewrite the equation for the lower plane actuator (similar equation for the upper plane actuator),

$$\dot{u}_{\ell i} = -\omega_d u_{\ell i} + \omega_d u_{\ell o}. \tag{23}$$

Subscript o denotes the output from the compensator and i denotes the input to the plant; the lag frequency $\omega_d=2\pi/\tau_d$. We attempted to integrate the above first-order equation by the explicit Euler scheme. The closed-loop solution is numerically unstable. We switch to the implicit Euler scheme,

$$u_{\ell i}^{(n+1)} = \frac{u_{\ell i}^{(n)} + \Delta t \omega_d u_{\ell o}^{(n+1)}}{1 + \Delta t \omega_d}, \tag{24}$$

which is numerically stable. For a lag time constant τ_a as large as 3×10^{-2}, C1 successfully stabilizes the system. Surprisingly, this time constant is significantly higher than that predicted by the linear stability result (see Fig. 7). With C3, the performance is only slightly better. We increase the lag time constant to $\tau_a=0.1$, ten times as large. In Fig. 14(c), we show the time response. The closed-loop system is unstable.

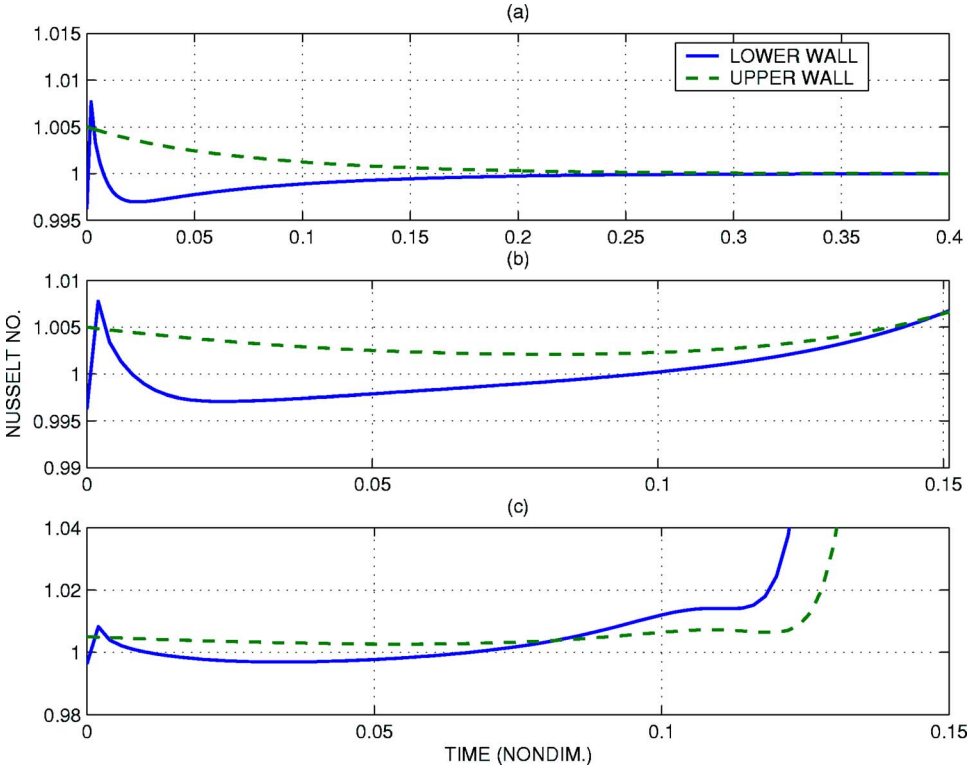

FIG. 14. (Color online) Case studies in the nonlinear simulations.

4. Major parameter uncertainties

The most benign major parameter mismatch by far is the Prandtl number. At nominal conditions, we can reduce Pr from 7.0 to 0.7 in the plant (compensator remains at Pr =7.0) without destabilizing the closed-loop time response.

For Rayleigh number, previous results indicate that the higher the nominal value Ra^* (here $\mathrm{Ra}^*=2\times10^4$), the smaller the plant uncertainty in Ra can be tolerated. Here, we let $\mathrm{Ra}=1.05\mathrm{Ra}^*$ (5% uncertainty), C1 is capable of stabilizing the no-motion state. However, when we set $\mathrm{Ra}=1.1\mathrm{Ra}_c^*$, now C1 is fighting very hard. We show the time response in Fig. 15(a). Considerable improvement is demonstrated by using C3 instead, as the time response shown in panel (b). But the system is still unstable. The Ra margin in the 3D

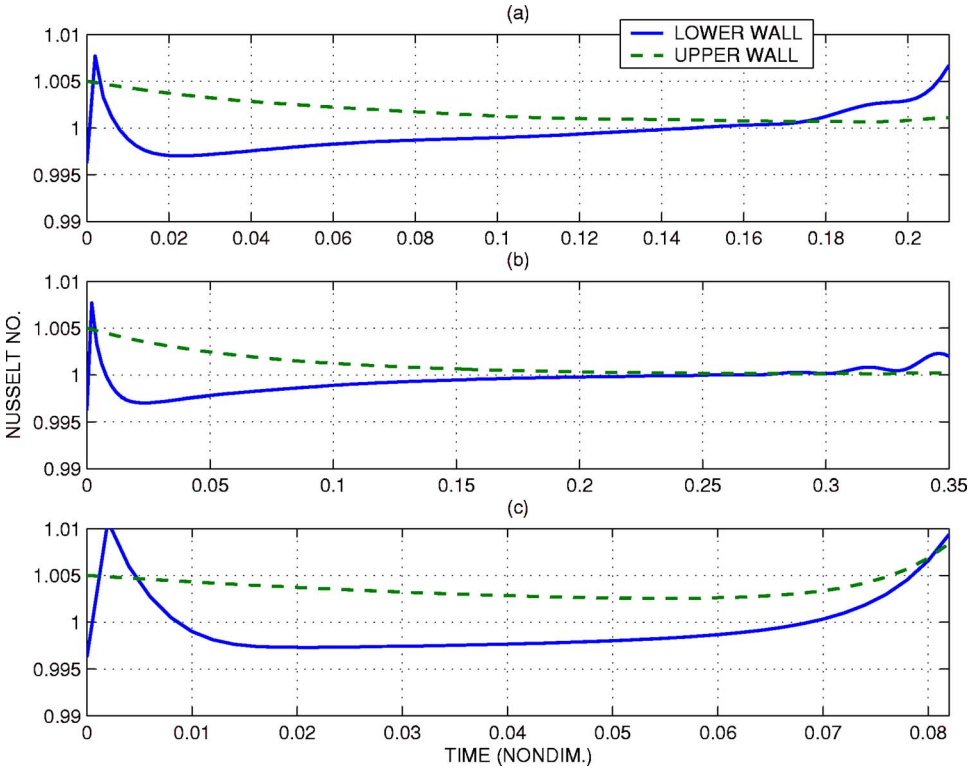

FIG. 15. (Color online) More case studies in the nonlinear simulations.

nonlinear model appears weaker than that predicted by the linear stability model (see Fig. 3).

5. Simulations with sensor plane level mismatch

Last, we consider the sensor plane level mismatch. The sensor level appears to be a sensitive parameter to the closed-loop stability. Even though we cannot run as many Monte Carlo cases as in the linear stability study (see Fig. 8), we ran several cases with level mismatch with standard deviation (STD) ±0.02 randomly (zero mean, Gaussian) added to the three nominal levels. The closed-loop responses remain stable. However, when we increase the mismatch STD to ±0.05, the closed-loop system is unstable. Figure 15(c) shows the time response for a case, with $z_s=0.15, 0.55$, and 0.85).

In examining the time responses of the Nusselt numbers, it seems puzzling at first to see that the convective disturbance is damped out to a very small amplitude in all cases initially, but the control action cannot sustain stability in some cases. The explanation is as follows. The initial time responses depend on the initial condition of the states. Since only one set of initial states is used, it is not surprising that the initial responses for all cases are similar. The simulation time appears adequate for the unstable modes to re-organize. The main point is that we have to simulate long enough to pass the initial transient period. The asymptotic response is what determine stability.

There is no specific mention about how the sensors can be implemented. It should be understood that the conventional, invasive-type of temperature sensors are probably not practical. Through private communications, however, it comes to our knowledge that certain infrared (IR) optical temperature sensing techniques (remote sensing) are available. Such optical remote-sensing method can probe temperatures at various depths in the layer, to very high accuracy. If the field-of-view of the sensor cannot cover the total horizontal span of the entire layer, a high-frequency scanning technique can be used to reconstruct the temperature field. For laboratory implementations, the remote-sensing method in measuring the temperatures should be further investigated.

IV. CONCLUSION

This study is to assess the amount of mismatches in the plant parameters (for a particular sensor and actuator configuration) that can be tolerated by the LQG compensator, before the closed-loop system turns unstable. This assessment is an important step towards any potential future laboratory implementation. The assessment is done by keeping the compensator operating at the nominal values and introducing mismatches to the plant model.

Based on the results from both the linear stability study and the nonlinear time-domain simulations, we draw the following conclusions: (i) Introducing the finite wall to the fluid layer does not have a significant impact in altering the closed-loop stability properties. The thermal conductive and diffusive properties of the walls in the study correspond to a good conducting material. The case of poor conducting material has not been considered. Therefore the idealized thermal boundary condition used in Refs. [5–8] appears adequate. The current results indicate that using the compensator C1 (with idealized boundary conditions) versus the finite-wall compensator C3 does not make any significant difference at all. For potential laboratory implementation, the dynamical model with idealized boundary conditions is probably adequate. (ii) Using two actuator planes on both walls does not show significant improvement in performance over using one actuator plane on the lower wall. Using two actuator planes reduces the load carried by one actuator plane. (iii) For the parameter mismatches in Rayleigh number, wall conductive and diffusive properties, wall thickness and sensor level locations, the linear stability results shows considerably larger margins than those obtained from the fully nonlinear simulations. For the actuator lag, however, it is the other way. The nonlinear results show more margins that from the linear results. Both linear and nonlinear results indicate that the Pr mismatch is insignificant. Mismatched Pr value anywhere in the range of 0.7–7.0 is tolerated. (iv) The more sensitive mismatches arise from the wall thicknesses and the sensor level locations. Both linear analysis and nonlinear simulations indicate that only small mismatches in these parameters can be tolerated at $\mathrm{Ra}=11.7\mathrm{Ra}_c$ (nominal value). Reducing the nominal Ra will reduce the sensitivity for given thickness and level mismatches.

In conclusion, the LQG compensator design is adequate to suppress convection in the vicinity of 10–15 times the critical Ra. The implementation of the actuator does not seem to be a challenge. The study shows that significant actuator lag can be tolerated. The major challenge appears to be in the sensors. The problem of sensitivity of stability margins to the sensor levels may require a novel temperature measurement technique to resolve. Rather than the invasive method, it is desirable to use the IR remote-sensing technique, coupled with a scanner approach. In principle, such technique can deliver temperature measurements at several levels of the fluid layer simultaneously, rapidly and accurately. Further investigation of the advanced sensing method is necessary for potential laboratory experiments.

ACKNOWLEDGMENT

This research was supported by the United States Air Force (Grant No. F49620-03-1-0244).

APPENDIX: CONDUCTIVE TEMPERATURE PROFILE

Let the outer surfaces of the upper and lower walls be prescribed at temperatures T_1^* and T_2^*, respectively. Let the layer thicknesses from below up be d_l^*, d^*, and d_u^*. Use the fluid layer thickness d^* and the temperature difference $\Delta T^* = T_2^* - T_1^*$ as the scales for length and temperature, respectively, so that we note the nondimensional variables (no asterisk) $T=T^*/\Delta T^*$, $z=z^*/d^*$, $T_1=T_1^*/\Delta T^*$, $T_2=T_2^*/\Delta T^*$, $d_l = d_l^*/d^*$, $d=1$, and $d_u=d_u^*/d^*$. Let T_3 and T_4 be the nondimensional temperatures at the inner upper and lower walls. The constant dimensional heat flux Q^* in the layers is given by

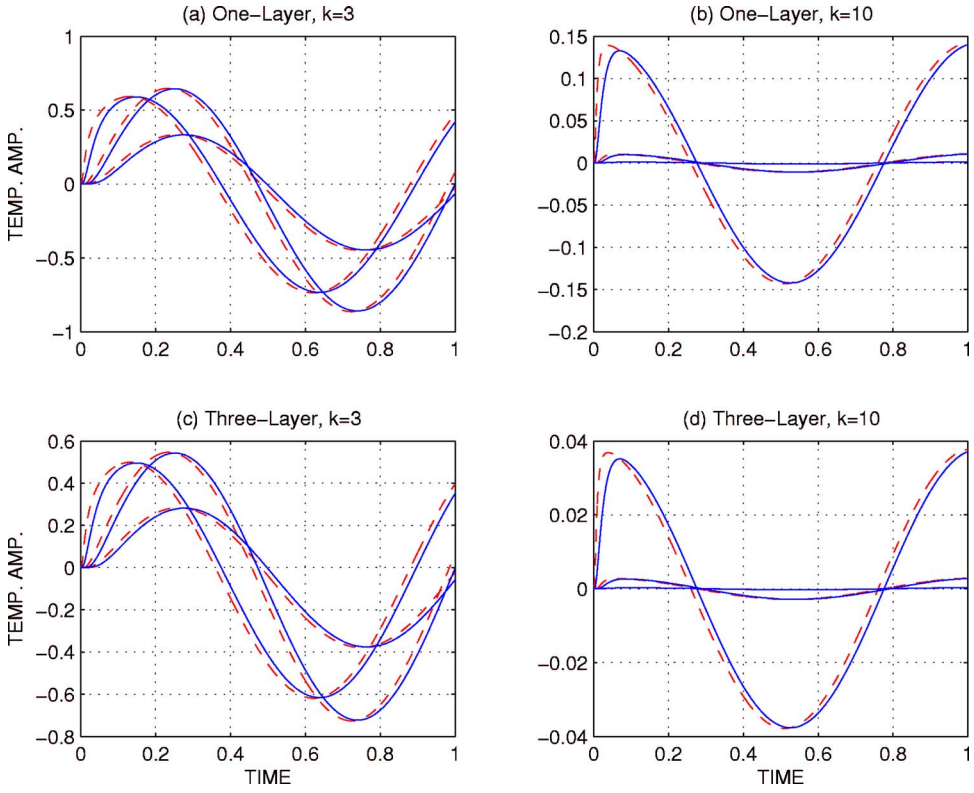

FIG. 16. (Color online) Sensor temperature comparison for one-layer vs three-layer, with (solid) and without (dashed) actuator lag.

$$Q^* = \frac{k^* \Delta T^*}{d^* h}, \quad h = 1 + d_u + d_l, \tag{A1}$$

where h is the nondimensional factor given in Eq. (A1). The temperatures T_3 (at upper wall inner surface) and T_4 (at lower wall inner surface) are

$$T_3 = T_1 + d_u/(k_u h), \quad T_4 = T_2 - d_l/(k_l h). \tag{A2}$$

We denote the thermal conductivity ratios $k_l = k_l^*/k^*$ and $k_u = k_u^*/k^*$. The temperature in the three layers as a function of z is

$$T(z) = \begin{cases} T_2 - (z + d_l)/(k_l h), & -d_l \leqslant z \leqslant 0, \\ T_4 + (T_3 - T_4)z, & 0 < z \leqslant 1, \\ T_1 + (1 + d_u - z)/(k_u h), & 1 < z \leqslant 1 + d_u. \end{cases} \tag{A3}$$

The effective Rayleigh number is the fluid interface-to-interface Rayleigh number. This number is given by $\mathrm{Ra}_f = \alpha^* g \Delta T^* (T_4 - T_3) d^{*3}/v^* \kappa^*$. We derive that

$$\mathrm{Ra}_f = \left(1 - \frac{d_l}{k_l h} - \frac{d_u}{k_u h}\right)\mathrm{Ra}, \tag{A4}$$

with $\mathrm{Ra}_f < \mathrm{Ra}$.

It is helpful to show the plant input-output relationship, at least for the linear case in subcritical condition. Consider $\mathrm{Pr} = 7.0$, $\mathrm{Ra} = 0.9\mathrm{Ra}_c$, let the nominal wall thermal conductivity and diffusivity values be reduced by 50% (for exaggeration). Consider a strong actuator lag with time constant $\tau_a = 0.1$. Consider a single, 2D Fourier mode of control at wave number of $k = 3$ and at $k = 10$. The control is the input temperature to the plant, with amplitude (Fourier coefficient) $u = \cos(2\pi f t)$ (here $f = 1$). The plant outputs are the temperature amplitudes at the nominal sensor plane levels $z_s = 0.2$, 0.5, and 0.8. Figure 16 shows the time responses of the control. On the left column, the upper and lower panel correspond to the one-layer and three-layer case, respectively. The wave number of the spatial sinusoidal disturbance is $k = 3$. The time responses in the two panels are very close, suggesting that, at least for the purely conductive case, the idealized wall and finite wall boundary conditions are about the same. The dashed curves (no lag, i.e., $\tau_a = 0$) are close to the solid curves (with lag, $\tau_a = 0.1$) despite the large actuator lag time constant. Note that the peaks shift to the right as zs is increased. However, for $k = 3$ the temperature maximum occurs at the midplane rather than at the sensor plane closest to the actuator. Similarly, we show the responses on the right column. The right column corresponds to the larger wave number, $k = 10$. For the small-scale control, the temperature amplitude rapidly attenuates when moved away from the actuator plane. Unlike in the case of $k = 3$, the temperature amplitude drops monotonically as z_s is increased. It suggests that small-scale control can exist only in the region close to the actuator plane.

[1] L. E. Howle, Phys. Fluids **9**, 1861 (1997).
[2] J. Tang and H. H. Bau, J. Fluid Mech. **363**, 153 (1998).
[3] L. E. Howle, Int. J. Heat Mass Transfer **40**, 817 (1997).
[4] J. Tang and H. H. Bau, Proc. R. Soc. London, Ser. A **447**, 587 (1994).
[5] A. C. Or, L. Cortelezzi, and J. L. Speyer, J. Fluid Mech. **437**, 175 (2001).
[6] A. C. Or and J. L. Speyer, J. Fluid Mech. **483**, 111 (2003).
[7] P. S. Marcus, J. Fluid Mech. **146**, 45 (1984).
[8] A. C. Or and J. L. Speyer, Phys. Rev. E **71**, 046302 (2005).
[9] L. E. Howle, J. Fluid Mech. **411**, 39 (2000).
[10] A. C. Or and R. E. Kelly, J. Fluid Mech. **440**, 27 (2001).
[11] J. C. Doyle and G. Stein, IEEE Trans. Autom. Control **AC-24**, 607 (1979).
[12] J. L. Speyer *et al.*, J. Guid. Control Dyn. **7**, 695 (1984).